arXiv:2509.15011v1 [cs.CV] 18 Sep 2025

Sea-ing Through Scattered Rays: Revisiting the Image Formation Model for Realistic Underwater Image Generation

Vasiliki Ismiroglou* Malte Pedersen Stefan H. Bengtson Andreas Aakerberg
Thomas B. Moeslund
Visual Analysis and Perception Laboratory, Aalborg University, Denmark
Pioneer Centre for Artificial Intelligence, Denmark
`{vasilikii, mape, shbe, anaa, tbm}@create.aau.dk`

Abstract

In recent years, the underwater image formation model has found extensive use in the generation of synthetic underwater data. Although many approaches focus on scenes primarily affected by discoloration, they often overlook the model's ability to capture the complex, distance-dependent visibility loss present in highly turbid environments. In this work, we propose an improved synthetic data generation pipeline that includes the commonly omitted forward scattering term, while also considering a nonuniform medium. Additionally, we collected the BUCKET dataset under controlled turbidity conditions to acquire real turbid footage with the corresponding reference images. Our results demonstrate qualitative improvements over the reference model, particularly under increasing turbidity, with a selection rate of 82. 5% by survey participants. Data and code can be accessed on the project page: vap.aau.dk/sea-ing-through-scattered-rays.

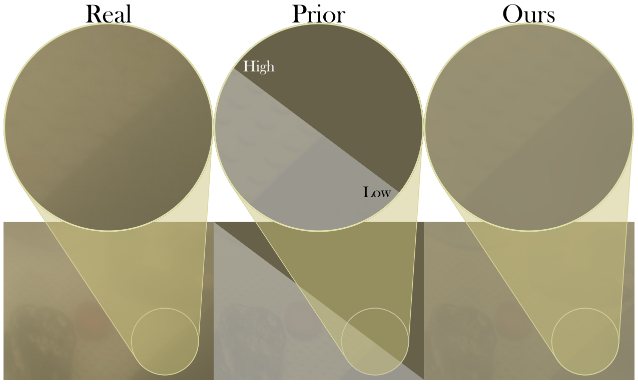

Figure 1. In high-turbidity environments, blur due to forward scattering is not negligible. Left: the real underwater image. Middle: results from a standard IFM using both low and high attenuation settings. Right: our proposed model under high attenuation. When attenuation is overestimated (middle), backscatter dominates before blur becomes perceptible. Best viewed when zoomed in.

1. Introduction

Underwater computer vision has gained significant momentum in recent years, driven largely by the growing urgency of environmental monitoring. As marine ecosystems face unprecedented threats from climate change, pollution, and overfishing, there is a need for tools that can support long-term ecological assessment and conservation efforts. Given the significant progress of data-driven methods in more common terrestrial applications, they present a strong foundation for addressing this problem. However, underwater settings come with unique challenges compared to their above-sea counterparts.

The physical underwater environment makes collecting data particularly hard. Among other things, getting recording equipment underwater is not trivial, as it requires specialized casings, divers, or expensive remotely operated vehicles (ROVs) and a degree of maintenance that is not always feasible or practical.

Another hindrance is the low visibility that comes as a result of the properties of the medium. Light is attenuated differently in water compared to the atmosphere, with longer wavelengths absorbed at very short depths, leading to discolorations of the footage [20]. Natural light does not penetrate the medium after a certain depth, making artificial lighting necessary. That in turn amplifies backscattering and introduces new degradations, such as uneven illumination [24, 29]. The attenuation caused by seawater is further intensified by the presence of suspended particles and sediment, commonly referred to as turbidity. Seawater composition is often described using the Jerlov classification scheme [11], which distinguishes between five coastal (1C, 3C, 5C, 7C, 9C) and five oceanic (I, IA, IB, II, III) water types based on optical depth. Coastal waters are gen-

---

*Corresponding author

erally more affected by turbidity.

Due to the challenges and high costs of collecting underwater footage, available data is sparse, with source locations heavily skewed towards clearer and 'interesting' habitats. In contrast, murky environments have been largely neglected.

Synthetic data generation has been widely proposed as a solution to data scarcity [15, 28], particularly in the domain of image enhancement and restoration, where access to reference images is crucial. One common approach uses the underwater image formation model (IFM) to simulate various underwater effects on clean images [4, 5, 8, 26, 28]. This method is computationally efficient and straightforward to implement. However, it often produces visually unrealistic results, especially in turbid conditions. We believe that this approach has been misrepresented in the literature, with oversimplified or inconsistent formulations and evaluation on only a limited subset of relevant environments.

In this work, we examine the subtle differences among IFM implementations and their impact on the synthesized images. Furthermore, we propose improvements with a particular focus on better modeling and synthesizing of high-turbidity environments. The contributions of this paper can be summarized as follows:

- A detailed review of prior work in synthetic data generation using the underwater IFM, highlighting important challenges that have not been adequately addressed.
- A dataset of induced turbidity in a controlled environment. The dataset showcases the effects of particulates in the water medium with respect to scene discoloration and information loss.
- An improved synthetic data generation pipeline that includes the commonly omitted *forward scattering* term of the underwater IFM and considers inhomogeneities in the medium. Qualitative results show that our method produces more realistic outputs than the default IFM, particularly in high turbidity conditions.

2. Related work

In this paper, the related work is categorized into two main areas to highlight their distinct focuses. The first, discussed in Sec. 2.1, concerns the development, evaluation, and refinement of the underwater IFM over time. The second area, presented in Sec. 2.2, centers on one of the model's common applications: the generation of synthetic data for learning-based methods.

2.1. Underwater image formation model

Only a portion of the light that gets reflected from an underwater scene towards a camera reaches the lens uninterrupted. The rest can be scattered at small angles within the field of view, scattered at larger angles and diverge from the camera, or be completely absorbed due to particles of varying sizes. Additionally, these particles can scatter light towards the camera before it even reaches the scene, providing no relevant information to the captured image.

These processes are typically approximated by the underwater image formation model, also known as the Jaffe-McGlamery model [10, 19]. In its simplified form, it is defined as:

$$\mathbf{I}(\mathbf{x}) = \mathbf{D}(\mathbf{x}) + \mathbf{F}(\mathbf{x}) + \mathbf{B}(\mathbf{x}) \tag{1}$$

where $\mathbf{I}(\mathbf{x})$ is the degraded image, $\mathbf{D}(\mathbf{x})$ is the direct transmission, $\mathbf{F}(\mathbf{x})$ is the small-angle forward scattering, and $\mathbf{B}(\mathbf{x})$ is the backscatter. **Bold letters** indicate 2-dimensional arrays representing images.

In [21], Schechner and Karpel argued that the effects of the forward scattering term are minimal and can be ignored. By assuming that forward scattering only introduces blur, they simplified the direct and forward components to be a signal of the form:

$$\mathbf{D}(\mathbf{x}) + \mathbf{F}(\mathbf{x}) = \mathbf{D}(\mathbf{x})_{blurred} \tag{2}$$

and showed that reduced contrast due to backscatter seemingly overpowers any blurring effects.

The direct transmission, $\mathbf{D}(\mathbf{x})$, is produced through attenuation of the latent true scene radiance, $\mathbf{J}(\mathbf{x})$, which represents the image that would be captured in the absence of water between the scene and the camera [19].

$$\mathbf{D}(\mathbf{x}) = \mathbf{J}(\mathbf{x}) \cdot \mathbf{t}(\mathbf{x}) = \mathbf{J}(\mathbf{x}) \cdot e^{-\beta_c^D \cdot \mathbf{z}(\mathbf{x})} \tag{3}$$

Here, $\mathbf{t}(\mathbf{x})$ denotes the transmission map, which is the proportion of scene radiance that reaches the camera lens after traveling through the water medium. It is modeled according to the Beer–Lambert law of exponential decay and is a function of the distance between the camera and the scene, $\mathbf{z}(\mathbf{x})$, as well as an attenuation coefficient β_c^D [2, 10, 19, 20].

$\beta(\lambda)$ is the collimated beam attenuation coefficient, and is an inherent optical property (IOP) of the medium [20]. It is the sum of an absorption, $a(\lambda)$, and a scattering, $b(\lambda)$, coefficient, both of which are dependent on the wavelength of light. Akkaynak et al. [2] showed that β_c^D is a function of $\beta(\lambda)$, along with the camera's spectral response and scene distance, and can diverge from the medium's IOPs.

Backscattering is modeled similarly:

$$\begin{aligned}\mathbf{B}(\mathbf{x}) &= \int_0^z b(\lambda) \cdot E(d,\lambda) \cdot e^{-\beta_c^B \cdot \mathbf{z}(\mathbf{x})} dz \\ &= B^\infty \cdot [1 - e^{-\beta_c^B \cdot \mathbf{z}(\mathbf{x}))}]\end{aligned} \tag{4}$$

and represents the characteristic hazy veil commonly observed in underwater imagery. B^∞ is the value of the veil at an infinite distance

$$B^\infty(\lambda) = \frac{b(\lambda)E(d,\lambda)}{\beta(\lambda)} \tag{5}$$

where $E(d, \lambda)$ is the ambient light at vertical depth d, this time calculated through the diffuse attenuation coefficient for downwelling irradiance $\mathcal{K}_d(\lambda)$:

$$E(d, \lambda) = E(0, \lambda) \cdot e^{-\mathcal{K}_d(\lambda) \cdot d} \tag{6}$$

Akkaynak et al. [1], showed that the backscattering attenuation coefficient β_c^B is a distinct function of $\beta(\lambda)$, and it differs from the direct transmission coefficient β_c^D, which had previously been assumed to be identical.

The forward scattering component has been modeled to have the following form [10, 19]:

$$\mathbf{F}(\mathbf{x}) = \left[\left(e^{-G(\lambda) \cdot \mathbf{z}(\mathbf{x})} - e^{\beta(\lambda) \cdot \mathbf{z}(\mathbf{x})} \right) \cdot \mathbf{J}(\mathbf{x}) \right] * \mathbf{H}(\mathbf{x}) \tag{7}$$

$$\mathbf{H}(\mathbf{x}) = \mathcal{F}^{-1}(e^{-\phi \cdot \mathbf{z}(\mathbf{x})}) \tag{8}$$

where $G(\lambda)$ and $\phi \geq 0$ are empirical, $*$ signifies convolution and $\mathcal{F}^{-1}$ is the inverse Fourier transform. Intuitively, this is a weighted and blurred version of $\mathbf{J}(\mathbf{x})$.

The papers of McGlamery [19] and Jaffe [10] disagree on the use of $\mathbf{J}(\mathbf{x})$ or $\mathbf{D}(\mathbf{x})$ for the calculation, with [19] specifying the former should be used, as it is the true source of the scattered particles. They also disagree on the empirical limits of $G(\lambda)$, with [19] proposing $a(\lambda) \leq G(\lambda) \leq \mathcal{K}_d(\lambda)$ and [10] proposing $|G(\lambda)| \leq \beta(\lambda)$.

When using $\mathbf{J}(\mathbf{x})$ in the forward scattering term, the effective attenuation coefficient of $\mathbf{D}(\mathbf{x}) + \mathbf{F}(\mathbf{x})$ is $G(\lambda)$. If $G(\lambda) \approx \beta(\lambda)$, the forward scattering term vanishes. However, as $\beta(\lambda)$ grows and $G(\lambda) < \beta(\lambda)$, the forward scattering term increases, *reducing the effective signal attenuation* in addition to the introduction of blur.

The analysis of Schechner and Karpel [21], along with the computational difficulty of the term and the discrepancies between [19] and [10], have led to the forward scattering term being overlooked in recent years. This omission persists despite the fact that the majority of scattering happens at angles less than 90° [25], potentially within the field of view of a camera. Forward scattering may significantly impact apparent attenuation, especially in turbid environments. Therefore, in this work, we reintroduce the term and study its effects in practice.

2.2. Synthetic data using the underwater IFM

The underwater IFM has been widely used to synthesize data, using source images from both terrestrial and underwater environments. Although transforming terrestrial images into underwater scenes and modifying the attenuation of already underwater images are technically distinct tasks, their primary differences lie in the illumination profile, lens distortions, and content of the source images. However, these aspects are not addressed by the IFM, which solely models light attenuation in the medium between the scene and the camera. Therefore, within the scope of the IFM, there is little justification for treating the two tasks as fundamentally different.

Hou et al. [8] use a simplified version of the IFM that resolves the need for distance information. They propose calculating the complete transmission map of *real* underwater images using the red channel prior [7] and applying it to terrestrial images. However, a transmission map should transfer shape information in the form of artifacts on the synthetically degraded images, an effect that does not appear in the resulting SUID dataset. It is thus assumed, that transmission coefficients were calculated instead. The synthesized images exhibit the characteristic blue-green tint typical of underwater footage, but lack horizontal depth dependence and the gradual fading observed over large distances.

The authors in [3, 14, 26] apply the underwater IFM on the NYU-depth V2 dataset [22], which provides depth maps. In all works, B^∞ is selected randomly within a range, effectively decoupling its color from the attenuation coefficients. This allows for greater flexibility and variability, though the resulting color can be uncharacteristic of underwater environments. In [3, 14], the attenuation coefficient is simplified to the medium's inherent value. In contrast, [26] computes it across the full wavelength spectrum, taking into account all other dependencies—though it does not distinguish between the direct and backscattering terms and uses β_c^D for both. All studies consider the effect of vertical depth; however, [3, 14] do not clearly explain how depth is incorporated, and [26] uses the beam attenuation coefficient in place of the diffuse attenuation coefficient.

Desai et al. [4], introduce the distinction between β_c^D and β_c^B as proposed by [1]. Working on the same NYU-depth V2 dataset [22], the resulting images appear to darken with changes in water type rather than showing increased turbidity, and lack the typical color distortions characteristic of underwater environments. It is unclear whether this visual deviation is due to the introduction of β_c^B, or to another aspect of their implementation.

Desai et al. [5] approach varying depth simulation through a downwelling term in the direct transmission, and analytical B^∞ calculation using $\mathcal{K}_d$. They synthesize the RSUIGM[1] dataset with source images from SUID [8], but do not clarify how distance information is obtained.

Utilizing the scene structure, Liu et al. [18] simulate uniform, parallel, and artificial light conditions. They apply their approach to the EUVP [9] dataset, with depth maps extracted using megaDepth [17] and random rescaling.

All aforementioned works have used the synthesized images to develop or evaluate image restoration frameworks. Their key implementation differences are summarized in Tab. 1.

---

[1] An underwater version of RSUIGM has been published by the authors in the context of a workshop challenge[13].

A critical look

In much of the prior work, examples shown for coastal water types exhibit minimal visible attenuation, likely due to significantly underestimated horizontal distances. When accurate distances are available, the synthesized images often appear increasingly artificial as attenuation coefficients rise. At the same time, evaluations tend to focus on heavily discolored but low-scattering scenes, typically overlooking the quality of more turbid data.

This trend extends to work focused directly on the IFM. Measurements and studies of physical processes, such as forward scattering and its effects, are typically based on oceanic water types. However, due to the exponential nature of attenuation, deviations from physical realism are less noticeable in low-turbidity environments, making it easier to overlook model inaccuracies.

Although prior work has claimed to cover the full range of Jerlov water types, it remains unclear whether these approaches can reliably generalize to scattering-dominated, turbid environments. Therefore, in this work, we specifically shift our focus to that regime.

3. Methods

Our proposed method involves the inclusion of the forward-scattering term in the underwater IFM along with coefficient adjustments. Additionally, we introduce a stochastic approach to medium inhomogeneity, allowing for synthetic data with higher variation.

Since code of prior work is not available, we define and implement the following reference model, on which we apply our modifications: The *revised IFM* with β_C^D, β_C^B and $\mathbf{B}(\mathbf{x})$ calculated for the entire range of wavelengths, as proposed by the authors in [1, 2], with the inclusion of downwelling attenuation, similar to [5]. The full pipeline is shown in Fig. 2

3.1. Small angle forward scattering

We reintroduce the forward scattering term of Eq. (7) into the underwater IFM, and parametrize $G_(\lambda)$ as:

$$G(\lambda) = a(\lambda) + g \cdot b(\lambda) \tag{9}$$

Here, $a(\lambda)$ and $b(\lambda)$ are the absorption and scattering coefficients described in Sec. 2.1 and $g \leq 1$ represents the portion of light scattered away from the line of sight (LOS) between the scene and the camera. This parametrization is consistent with recent studies in water optical properties [6, 25].

Similarly, we change the effective attenuation coefficient of the backscattering term to match $G(\lambda)$. This choice is important for consistency, i.e., if we assume some of the scattered rays from the scene reach the lens, the same must be true of backscattered rays.

$$\mathbf{B}(\mathbf{x}) = B^{\infty} \cdot [1 - e^{-G_c^B \cdot \mathbf{z}(\mathbf{x})}] \tag{10}$$

Finally, we reduce the scattering coefficient in the backlight calculation (Eq. (5)) through constant $\mu \leq 1$, which is not necessarily the same as g. This reflects the assumption that not all light scattered by particles is initially directed toward the camera, even before accounting for attenuation along the LOS. The final backlight calculation is performed as follows:

$$B^{\infty}(\lambda) = \frac{\mu \cdot b(\lambda) \cdot E(d, \lambda)}{G(\lambda)} \tag{11}$$

Notice the use of $G(\lambda)$ which results from the integration in Eq. (4). The convolution in Eq. (7) is performed directly in the image domain, with a depth-variable Gaussian kernel and $\sigma = \phi \cdot \mathbf{z}(\mathbf{x})$.

3.2. Medium non-uniformity

A core assumption of the underwater IFM model is that the medium is uniform. Unlike marine snow, which consists of relatively large, visible particles, the non-uniformity referred to here arises from subtle, indistinguishable variations in the water that cause local fluctuations in absorption and scattering coefficients. These inhomogeneities cannot be analytically modeled or reliably approximated, as they are the result of chaotic fluid dynamics in unbounded volumes without clearly defined sources or initial conditions. Nonetheless, incorporating such randomness and variability can have a significant impact on the realism and effectiveness of synthetic data generation.

Work	Data type	$\mathbf{z}(\mathbf{x})$	B^{∞}	d	$\mathbf{F}(\mathbf{x})$	Availability
[8]	Terrestrial	-	Extracted	No	No	Dataset
[3, 14]	Terrestrial	Kinect	Rand. homog.	Undefined	No	-
[26]	Terrestrial	Kinect	Rand. homog.	$b(\lambda)$	No	-
[4]	Terrestrial	Kinect	Analytical	Undefined	No	-
[5]	Both	Undefined	Analytical	$\mathcal{K}_d$	No	Dataset
[18]	Underwater	megaDepth [17]	Analytical	Incident	No	-
Ours	Underwater	DepthAnythingv2[30]	Analytical	$\mathcal{K}_d$	Yes	Code

Table 1. Existing variations of synthetic data generation pipelines based on the underwater IFM. The column *Availability* corresponds to either the synthesized dataset or code availability, that would allow for the full range of outputs to be accessed.

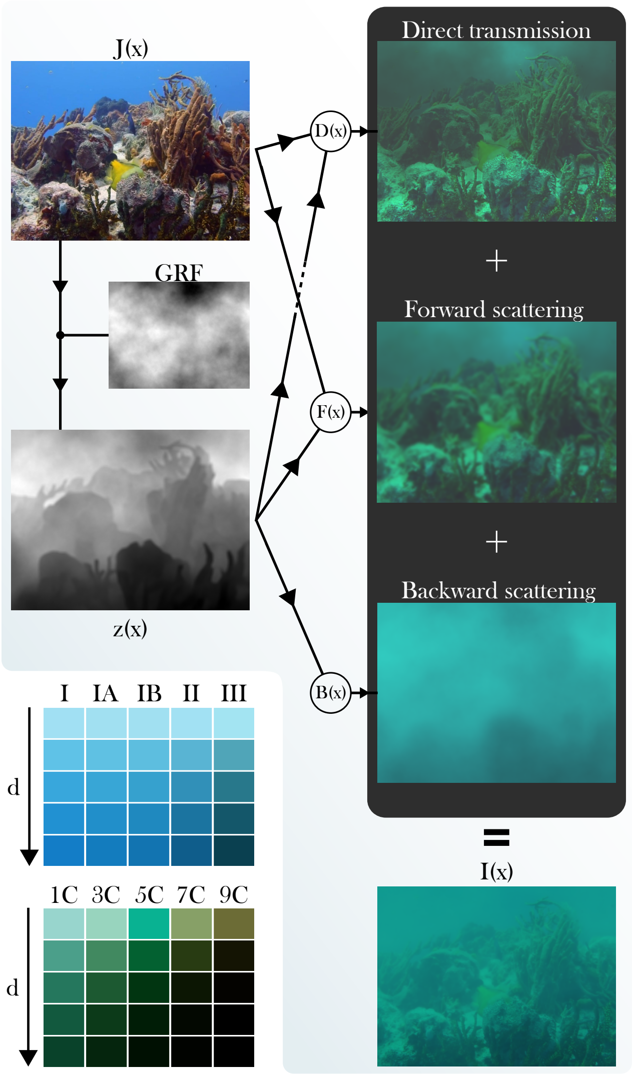

Figure 2. The proposed synthetic data generation pipeline. The inputs are a clear underwater image, along with a depth map multiplied with a Gaussian Random Field. The direct, forward, and backscattering components are calculated using the desired water type coefficients through their respective functions, Eqs. (3), (4) and (7). Their sum is the degraded image **I(x)**. The white-patch behavior for all Jerlov water types [23] is displayed on the bottom left. **The direct and forward scattering images have had their contrast and brightness enhanced for visualization purposes.*

Gaussian random fields (GRFs) have been used to describe natural physical processes, such as the deviations in homogeneity of the Cosmic Microwave Background [27], and have also been applied in generating synthetic image data [16]. Specifically, scale-free Gaussian Random Fields have a fractal structure with spatial correlations on different scales, and visually resemble smoke effects. A GRF is generated for every image and its values are scaled to small variations around 1. It is then multiplied by the depth map, which effectively corresponds to density variations.

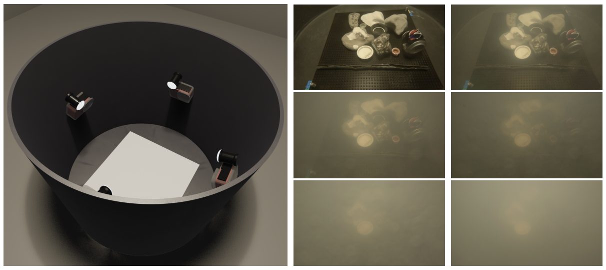

(a) (b)

Figure 3. The BUCKET dataset. a) The data collection setup. b) Some example images at increasing turbidity.

It is important to note that this process is not proposed as an extension of the underwater IFM, but rather as a general-purpose degradation technique.

4. Experiments and results

4.1. The BUCKET dataset

A reappearing problem in synthetic image generation is the lack of ground truth. Without a ground truth, it is not trivial to evaluate the quality of the result. Motivated by this, we propose an image dataset, the *Baseline for Underwater Conditions in Known Environments and Turbidity (BUCKET)*.

The data collection setup involves four *GoPro* cameras, equally spaced along the perimeter of a cylindrical tank with opaque walls. All data collection took place in a dark room, and lighting was introduced through four *Blue Robotics Lumen* subsea lights and a diffused lamp centered above the tank. Turbidity was simulated using increasing amounts of oat milk and clay, and was accurately measured. On the bottom of the tank, sets of objects were placed on a *LEGO* baseplate, retaining object positions. This ensures the preservation of the scene between the clear reference images and the ones collected as turbidity increases. Objects include, but are not limited to, artificial and real rocks, as well as trash of different shapes and colors. A visualization of the setup, along with sample images, is presented in Fig. 3.

The setup and collection protocol were designed to generate a diverse range of conditions, enabling the resulting images to support multiple underwater vision tasks, such as image restoration, object detection, and multi-view reconstruction. A total of 64 images, captured only under ambient light from the overhead lamp, comprise a preliminary version of the dataset and are considered in this work. They will be made publicly available through the project page.

4.2. Comparison with reference images

To obtain usable depth information for the collected footage, we employed the state-of-the-art monocular depth estimation model, Depth-Anything-v2 [30], and generated depth maps from the clean images. The predicted relative depths were then scaled using the known setup dimensions.

Since the induced turbidity does not correspond precisely to any standard Jerlov water type, coefficients were approximated to visually match the ground truth images: $\beta_c^D = \beta_c^B = \beta_c^{approx}$. As such, this is a simplified version of the reference model defined in Sec. 3. Detailed values are provided in the supplementary material.

Fig. 4 shows a comparison of real and synthetic images. The turbidity measurements for the real underwater images are 1.2, 6.53, 16.07, 20.20, and 30.43 NTU, respectively, and the added substance was oatmilk. All synthesized images share a horizontal depth range of 0.3-0.7m and a vertical depth of 0.5m.

4.3. Evaluation survey

In order to evaluate the proposed pipeline on images without references, we collected the mean opinion ranking (MOR) through a survey. Images were randomly selected from the EUVP dataset [9], and manually filtered to remove any footage that was either not clear enough or with a horizontal depth too short to showcase the effects of turbidity (e.g., zoomed-in pictures of a fish). A subset of these images was then randomly split into 9 groups of 2, corresponding to the water types IA-9C. Water type I was skipped due to its high similarity with IA and low overall degradation.

Images had their conditions synthetically altered with both the reference model and ours, resulting in 18 pairs. The vertical and horizontal depths were set to 1m and 1-5m, respectively, across all images in the survey. These values are not necessarily accurate for all images, but the process is representative of randomized data generation at scale. For each water type, coefficients were taken from [23], and the spectral response of a *Nikon D90* was considered [12]. All other model parameters are listed in Tab. 2

The 20 survey participants were experienced in the field of computer vision and potentially familiar with synthetic data, though not necessarily with underwater environments. They were shown a set of unedited underwater images of different conditions at the start of the survey as a reference, and were then asked to choose the most realistic image for each pair. The order in which choices appeared was randomized. All survey images can be found in the supplementary, while results are displayed in Fig. 6.

Randomly scaling the horizontal depth, as done here and in prior work [18], can have undesirable outcomes. To study this effect, we alter depth scaling on an image from the

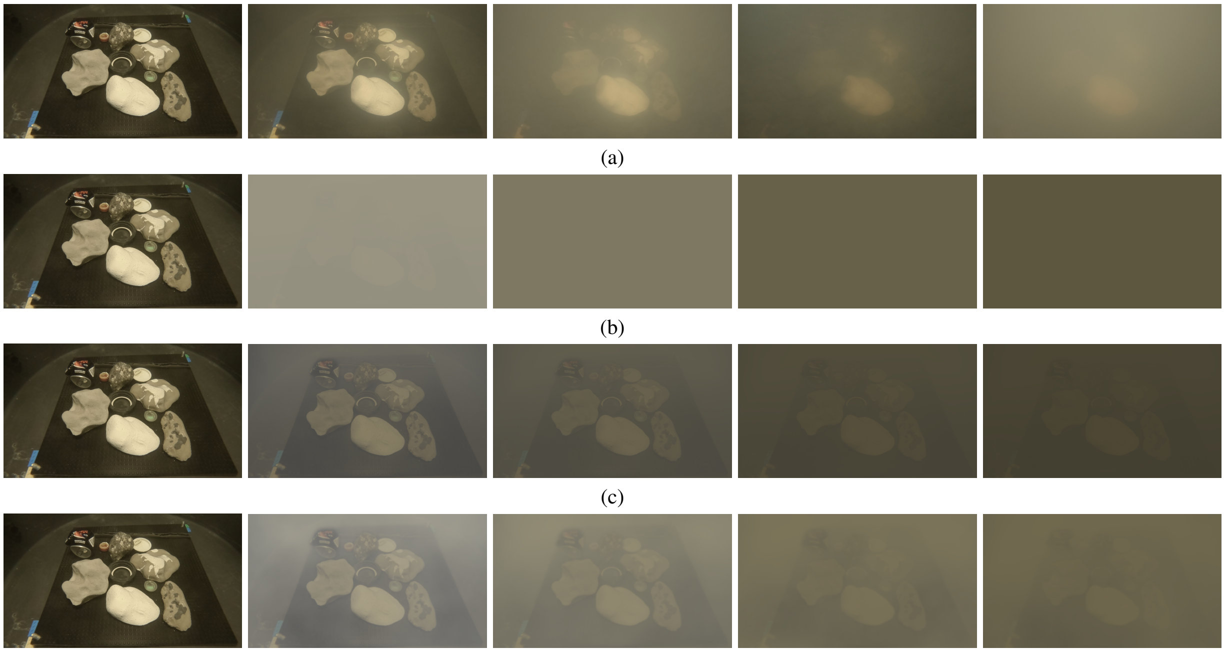

(a)

(b)

(c)

(d)

Figure 4. Comparison of the underwater IFM with real data. Columns indicate increasing turbidity. a) Real underwater data. b) Synthetic data with the reference model. c) Synthetic data with the reference model but $b_c^{eff} = g \cdot b_c^{approx}$. d) Synthetic data with the proposed model. Rows c and d share the same effective attenuation coefficients. However, d includes blur, inhomogeneity effects, and a backlight adjusted through μ. Our proposed model is not equivalent to only reducing the scattering coefficient.

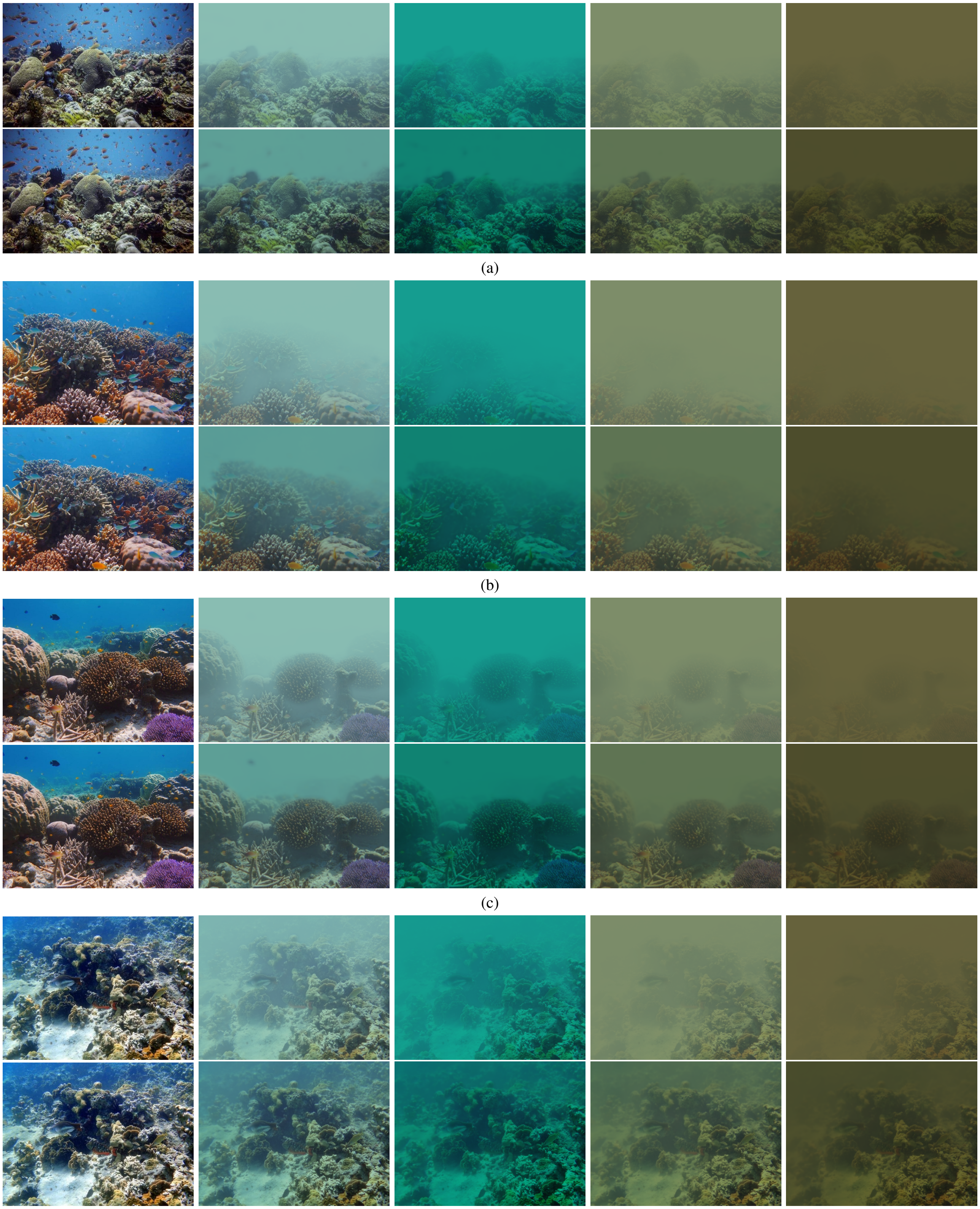

(a)

(b)

(c)

(d)

Figure 5. Example synthesized images for Jerlov water types 3C-9C [23]. The first column is the clean source image [9]. For each figure (a–d): top row shows the reference model; bottom row shows our proposed model. Differences are best observed when zoomed in.

g	μ	ϕ	GRF
0.2	0.3	$0.3 \cdot \bar{b}$	$[0.7 - 1.3]$

Table 2. Model parameters. $\bar{b}$ is the mean across all channels.

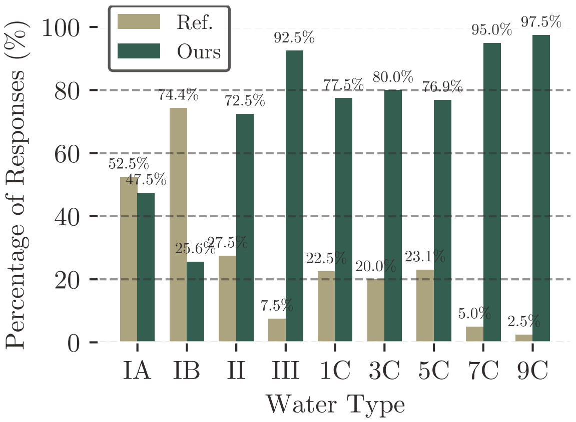

Figure 6. Survey results. Question: *Given some examples of real underwater images, choose the one that looks more realistic.*

Figure 7. Effect of depth scaling. Simulation of type II and 7C waters is shown next to the scaled depth map. Top row: 0-20m with linear scaling. Middle row: 0-20m with a gamma value of 3. Bottom row: 0-20m with a gamma value of 6.

EUVP dataset [9], while maintaining all other parameters consistent. The results can be seen in Fig. 7. Finally, a few example images with customized depth and parameters can be seen in Fig. 5.

5. Discussion

Contrary to the conclusions of [21], our experiments show that image blur is noticeable, even at short distances in turbid conditions. This can be seen in Fig. 4, and is highlighted in Fig. 1, particularly around edges and the baseplate details. While part of this discrepancy can be attributed to the empirical constant ϕ in Eq. (7), we believe it is also largely due to an overestimated attenuation.

As scattering coefficients increase, the reference model assumes a large β, resulting in a heavily reduced direct signal and overpwoering backscatter. However, when considering that the scattered rays reaching the camera contain information and not only "blur", the effective attenuation decreases enough for the blur to be visible.

Within this framework of effective scattering coefficients corresponding to specific scattering angle ranges, the backlight and attenuation intensities can be decoupled to some degree. That is contained within constant μ (Eq. (11)), which introduces more flexibility and variation to the reference $\frac{b(\lambda)}{\beta(\lambda)}$ term. The practical implications can be seen in Fig. 4, particularly, in the way the last two rows diverge. They both have the same attenuation, but row *d* has a brighter backlight, similar to the ground truth.

Focusing on visual realism, applying GRFs to the depth maps helps the added effects blend more naturally, with transitions that are smoother and less tightly bound to object edges. This results in more gradual and realistic fading. GRFs also help mitigate common artifacts from learning-based depth estimators, such as overly smooth or artificially rounded edges.

Results of the evaluation survey support our claims about realism, with our proposed pipeline being preferred over the reference in 73.9% of the responses across all water types and 82.5% for coastal ones. Notably, the decline in participant choice separation between water types IA and II coincides with a decrease in the forward scattering term, making visual differences increasingly imperceptible.

Despite the improvements, accurate depth remains a weak point of this approach to synthesizing data. Fig. 7 showcases the large divergence between images as the depth scaling is altered. Note how the minimum and maximum values remain identical, and it is only a gamma term that is modified. The potential impact that inaccurate depth can have on downstream tasks remains to be studied.

6. Conclusion

In this work, we introduced an improved synthetic underwater data generation process based on the IFM. It incorporates medium inhomogeneity and the forward scattering term, which is commonly overlooked in traditional models. Qualitative evaluations demonstrate that by integrating these components into the pipeline, our approach yields significantly more realistic results, particularly in turbid conditions.

7. Acknowledgments

This work was funded by the Pioneer Centre for Artificial Intelligence in Denmark.

References

[1] Derya Akkaynak and Tali Treibitz. A Revised Underwater Image Formation Model. In *2018 IEEE/CVF Conference on Computer Vision and Pattern Recognition*, pages 6723–6732, 2018. ISSN: 2575-7075. 3, 4

[2] Derya Akkaynak, Tali Treibitz, Tom Shlesinger, Yossi Loya, Raz Tamir, and David Iluz. What is the Space of Attenuation Coefficients in Underwater Computer Vision? In *2017 IEEE Conference on Computer Vision and Pattern Recognition (CVPR)*, pages 568–577, 2017. ISSN: 1063-6919. 2, 4

[3] Saeed Anwar, Chongyi Li, and Fatih Porikli. Deep Underwater Image Enhancement, 2018. arXiv:1807.03528 [cs]. 3, 4

[4] Chaitra Desai, Ramesh Ashok Tabib, Sai Sudheer Reddy, Ujwala Patil, and Uma Mudenagudi. RUIG: Realistic Underwater Image Generation Towards Restoration. In *2021 IEEE/CVF Conference on Computer Vision and Pattern Recognition Workshops (CVPRW)*, pages 2181–2189, Nashville, TN, USA, 2021. IEEE. 2, 3, 4

[5] Chaitra Desai, Sujay Benur, Ujwala Patil, and Uma Mudenagudi. RSUIGM: Realistic Synthetic Underwater Image Generation with Image Formation Model. *ACM Trans. Multimedia Comput. Commun. Appl.*, 21(1):10:1–10:22, 2024. 2, 3, 4

[6] David Doxaran, Edouard Leymarie, Bouchra Nechad, Ana Dogliotti, Kevin Ruddick, Pierre Gernez, and Els Knaeps. Improved correction methods for field measurements of particulate light backscattering in turbid waters. *Optics Express*, 24(4):3615–3637, 2016. Publisher: Optica Publishing Group. 4

[7] Adrian Galdran, David Pardo, Artzai Picón, and Aitor Alvarez-Gila. Automatic Red-Channel underwater image restoration. *Journal of Visual Communication and Image Representation*, 26:132–145, 2015. 3

[8] Guojia Hou, Xin Zhao, Zhenkuan Pan, Huan Yang, Lu Tan, and Jingming Li. Benchmarking Underwater Image Enhancement and Restoration, and Beyond. *IEEE Access*, 8: 122078–122091, 2020. Conference Name: IEEE Access. 2, 3, 4

[9] Md Jahidul Islam, Youya Xia, and Junaed Sattar. Fast Underwater Image Enhancement for Improved Visual Perception, 2020. arXiv:1903.09766 [cs]. 3, 6, 7, 8

[10] J.S. Jaffe. Computer modeling and the design of optimal underwater imaging systems. *IEEE Journal of Oceanic Engineering*, 15(2):101–111, 1990. 2, 3

[11] N. G. Jerlov. *Optical studies of ocean waters*. Elanders boktr., Goteborg, 1957. 1

[12] Jun Jiang, Dengyu Liu, Jinwei Gu, and Sabine Susstrunk. What is the space of spectral sensitivity functions for digital color cameras? In *2013 IEEE Workshop on Applications of Computer Vision (WACV)*, pages 168–179, Clearwater Beach, FL, USA, 2013. IEEE. 6

[13] Benjamin Kiefer, Lojze Zust, Matej Kristan, Janez Pers, Matija Tersek, Uma Mudenagudi, Chaitra Desai, Arnold Wiliem, Marten Kreis, Nikhil Akalwadi, Zhiqiang Zhong, Zhe Zhang, Sujie Liu, Xuran Chen, Yang Yang, Matej Fabijanic, Fausto Ferreira, Seongju Lee, Shanliang Yao, Himanshu Kumar, Aurelius Marcus, Gregor Novak, Yuan Feng, Annie Cheng, Thien Nguyen, Jannik Sheikh, Josip Saric, Zhuoxiao Li, Yutang Lu, Yipeng Lin, Xiang Yang, Ching-Heng Cheng, Ali Awad, Jon Muhovic, Yitong Quan, Junseok Lee, Kyoobin Lee, Runwei Guan, Xiaoyu Huang, Yi Ni, Tzu-Yu Lin, Chia-Ming Lee, Chih-Chung Hsu, Andreas Michel, Wolfgang Gross, Nan Jiang, Fei Feng, Evan Lucas, Ashraf Saleem, Yu-Fan Lin, and Martin Weinmann. 3rd Workshop on Maritime Computer Vision (MaCVi) 2025: Challenge Results. 3

[14] Chongyi Li, Saeed Anwar, and Fatih Porikli. Underwater scene prior inspired deep underwater image and video enhancement. *Pattern Recognition*, 98:107038, 2020. 3, 4

[15] Jie Li, Katherine A. Skinner, Ryan M. Eustice, and Matthew Johnson-Roberson. WaterGAN: Unsupervised Generative Network to Enable Real-time Color Correction of Monocular Underwater Images. *IEEE Robotics and Automation Letters*, pages 1–1, 2017. 2

[16] Xin Li, Yanni Dong, Junge He, Xin Yang, Wenlong Zhou, and Xiangyun Hu. Multimodal U-Net: A Novel Approach for 2-D Inversion of Magnetotelluric Data. *IEEE Transactions on Geoscience and Remote Sensing*, 63:1–12, 2025. 5

[17] Zhengqi Li and Noah Snavely. MegaDepth: Learning Single-View Depth Prediction from Internet Photos. In *2018 IEEE/CVF Conference on Computer Vision and Pattern Recognition*, pages 2041–2050, Salt Lake City, UT, USA, 2018. IEEE. 3, 4

[18] Yidan Liu, Huiping Xu, Bing Zhang, Kelin Sun, Jingchuan Yang, Bo Li, Chen Li, and Xiangqian Quan. Model-Based Underwater Image Simulation and Learning-Based Underwater Image Enhancement Method. *Information*, 13(4):187, 2022. 3, 4, 6

[19] B. L. McGlamery. A Computer Model For Underwater Camera Systems. In *Ocean Optics VI*, pages 221–231. SPIE, 1980. 2, 3

[20] Curtis Mobley. *Light and Water: Radiative Transfer in Natural Waters*. 1994. Journal Abbreviation: Academic Press Publication Title: Academic Press. 1, 2

[21] Y.Y. Schechner and N. Karpel. Clear underwater vision. In *Proceedings of the 2004 IEEE Computer Society Conference on Computer Vision and Pattern Recognition, 2004. CVPR 2004.*, pages 536–543, Washington, DC, USA, 2004. IEEE. 2, 3, 8

[22] Nathan Silberman, Derek Hoiem, Pushmeet Kohli, and Rob Fergus. Indoor Segmentation and Support Inference from RGBD Images. In *Computer Vision – ECCV 2012*, pages 746–760, Berlin, Heidelberg, 2012. Springer. 3

[23] Michael G. Solonenko and Curtis D. Mobley. Inherent optical properties of Jerlov water types. *Applied Optics*, 54(17): 5392–5401, 2015. Publisher: Optica Publishing Group. 5, 6, 7

[24] K. Sooknanan, A. Kokaram, D. Corrigan, G. Baugh, J. Wilson, and N. Harte. Improving underwater visibility using vignetting correction. page 83050M, Burlingame, California, USA, 2012. 1

[25] Noah Tuchow, Jennifer Broughton, and Raphael Kudela. Sensitivity analysis of volume scattering phase functions. *Optics Express*, 24(16):18559–18570, 2016. Publisher: Optica Publishing Group. 3, 4

[26] Takumi Ueda, Koki Yamada, and Yuichi Tanaka. Underwater Image Synthesis from RGB-D Images and its Application to Deep Underwater Image Restoration. In *2019 IEEE International Conference on Image Processing (ICIP)*, pages 2115–2119, 2019. ISSN: 2381-8549. 2, 3, 4

[27] Benjamin D. Wandelt. Gaussian Random Fields in Cosmostatistics. In *Astrostatistical Challenges for the New Astronomy*, pages 87–105. Springer, New York, NY, 2013. 5

[28] Nan Wang, Yabin Zhou, F. Han, H. Zhu, and Yaojing Zheng. UWGAN: Underwater GAN for Real-world Underwater Color Restoration and Dehazing. *ArXiv*, 2019. 2

[29] Yulin Wang, Yueming Ma, Yuanyuan Li, Jiqing Zhang, Zetian Mi, and Xianping Fu. Underwater Vignetting Image Correction Based on Binary Polynomial Regularization and Latent Low-Rank Representation. *IEEE Transactions on Circuits and Systems for Video Technology*, 35(4):3410–3425, 2025. 1

[30] Lihe Yang, Bingyi Kang, Zilong Huang, Zhen Zhao, Xiaogang Xu, Jiashi Feng, and Hengshuang Zhao. Depth Anything V2, 2024. arXiv:2406.09414 [cs]. 4, 6